ACS OMEGA

Open Access

http://pubs.acs.org/journal/acsodf

Article

Thermal Insulation Properties and Simulation Analysis of Foam Concrete Regulated by Mechanical and Chemical Foaming

Hailin Jia,* Qian Zou, Bo Cui, and Jinxiang Zeng

Cite This: *ACS Omega* 2023, 8, 48091−48103

Read Online

ACCESS | Metrics & More | Article Recommendations

ABSTRACT: To address, mitigate, or prevent thermal environmental issues arising from the heat dissipation of high-temperature surrounding rocks in deep hot tunnels, a research proposal is put forward based on previous studies and the team's initial experiments. The proposal involves using mechanical and chemical foaming to enhance the thermal insulation properties of foamed concrete, and this will be tested through engineering verification. Different proportions of cementitious materials, latex powder, polypropylene fiber, and self-made composite foam materials were designed using an orthogonal approach for testing the macroperformance and microstructure of foamed concrete. The pore structure of foamed concrete was quantitatively analyzed by Image-Pro Plus 6.0 software, and a fitting expression was established between thermal conductivity and the number of pores (1−2 mm). Characteristics of heat transfer inside the foam concrete were simulated and analyzed using COMSOL software, and the transmission path of heat streamline was found to be "concave-convex form", illustrating the blocking effect of foam concrete on heat. A thermal insulation engineering model was created using Fluent software to investigate the effects of thermal insulation layer thickness, water gushing heat release, seasonal factors, and other working conditions on the airflow temperature in the roadway before and after the application of foam concrete. The simulation results demonstrate that foam concrete can effectively reduce the airflow temperature in the roadway and weaken the surrounding rock heat dissipation. Additionally, it is found that the decreasing rate of heat dissipation of surrounding rock increases with the increase of insulation layer thickness, proving the engineering applicability of foam concrete for roadway insulation. The research results provide a theoretical basis and practical guidance for heat damage control of deep mining roadway.

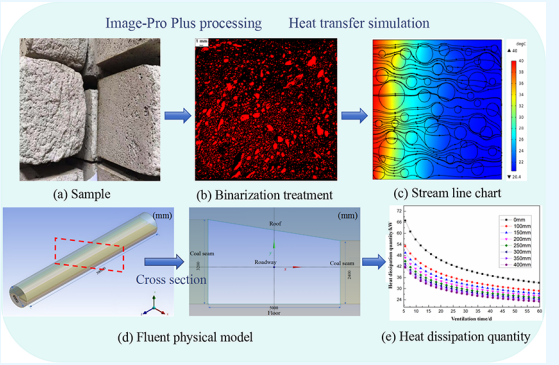

1. INTRODUCTION

With the progress of economy and society, the demand for coal mining and consumption has increased consecutively every year.[1,2] This has resulted in the depletion of shallow coal resources and forced the industry to transition to deeper coal mining.[3] The challenge of high-temperature heat damage related to deep mining has severely tested the physical and mental health of employees, as well as the safe and efficient extraction of coal.[4−8] In order to effectively prevent the problem of heat damage caused by high temperatures, a more scientific approach is to implement a management system which incorporates "heat insulation + heat dissipation" measures.

Currently, thermal hazard management in mines primarily centers on "heat dissipation". Considerable advancements have been made in cooling theory,[9,10] cooling technology,[11] and cooling equipment.[12] Both mechanical refrigeration and cooling solutions (such as cold air, cold water, and cold ice),[13−17] as well as nonmechanical cooling solutions (such as system optimization and increased airflow),[18−23] have been developed. Although these programs have enhanced the mine's operating environment, the efficacy of mine cooling remains limited due to challenges such as increased mining depth, system complexity, long distances for cold transmission, frequent location changes, significant cold loss, and difficulty discharging condensation heat. Given the constraints of implementing passive heat dissipation techniques, the concept of environmentally friendly mining and reducing energy consumption and emissions has prompted the adoption of thermal insulation materials to postpone or limit high temperatures of the surrounding rocks in the deep, hot mine tunnels. Insulation materials are commonly classified into two groups: organic and inorganic. However, the use of organic insulation materials in underground spaces is restricted due to their high susceptibility to fire hazards. Inorganic insulation materials, particularly foam concrete

Received: September 11, 2023
Revised: November 13, 2023
Accepted: November 22, 2023
Published: December 8, 2023

Table 1. Main Parameters and Functions of Each Raw Material

materials	manufacturers	main parameters	selection basis and function
portland cement	Henan Dengfeng Dengdian Group Cement Co., Ltd.	specific surface area (m^2/kg) ≥ 400 initial coagulation < 25 min 3 d compressive strength of 42.5 MPa	mix with water to form a cement slurry, which is the main cementitious material for the whole system after hardening
fly ash	Jiaozuo thermal power plant	grade of II fineness ≤ 12%	give play to volcanic ash effect, shape effect and ball effect
aggregate	Jiaozuo river sand	fineness is 2.8 particle size is 0.4 mm	play a role in supporting and filling internal pores, and reduce the shrinkage and cracking of foam concrete in the later stage
latex powder	Jinzhou Honghai cellulose co., ltd	density is 500 (g/L) the average particle size is 80 μm	strengthen the bond strength of cement mortar, improve cohesion, prevent early cracking of materials and improve durability
polypropylene fiber	Changzhou Bochao Engineering Material Co., Ltd.	the diameter length is 12 mm tensile strength > 300 MPa	the skeleton effect and bridging effect can effectively inhibit the cracking of cement paste and improve its strength and impact resistance
accelerator	Mengzhou Yulin Fine Chemical Plant	the content of calcium chloride is 75%	promote the initial setting time of cement slurry and the stability time of foam to achieve dynamic equilibrium

materials, are gaining significant interest among researchers due to their noncombustibility and thermal insulation properties.[24−32] A review of the literature indicates that foam concrete is predominantly prepared using mechanical foaming methods[33−35] or chemical foaming techniques.[36,37] He et al. produced alkali-activated slag foamed concrete with a dry density of 600−800 kg/m^3 using mechanical foaming, and it was observed that as the foam content increased, the thermal conductivity of the foamed concrete gradually decreased.[38] However, the addition of preformed foam to concrete slurry through mechanical foaming results in compromised foam durability due to the mixing and pouring processes. Hajimohammadi et al. used the same amount of aluminum powder as foaming agent to synthesize geopolymer foam with different porosity.[39] She et al. presented a novel method for the preparation of highly stable wet foams by simultaneously using NS particles, hdroxypropyl methylcellulose (HPMC), and a betaine surfactant.[40] Fei-fan et al. utilized the Fluent software to conduct a numerical simulation on thermal insulating concrete with an optimal, self-mixed thermal conductivity.[41] They discovered that this concrete exhibited a significant thermal insulation effect when used for laying mine tunnels.

From the analysis above, it is evident that foam concrete can be produced by using both mechanical and chemical foaming methods. However, mechanical foaming has a slow initial pore formation rate, while chemical foaming allows for early and rapid foaming, but with a limited time frame that requires careful control. Accordingly, this paper presents an experimental study on the preparation of foam concrete with the coordinated control of mechanical and chemical foaming. This study includes analysis of the thermal insulation performance and simulation, attempts to establish a quantitative treatment method of the internal pore structure of foam concrete, constructs empirical expressions of thermal conductivity coefficient and foam pore, and researches and analyzes the characteristics of heat transfer of heat in the interior of foam concrete. Based on an actual deep hot shaft, an engineering simulation was performed to analyze the changes in heat dissipation from surrounding rock and the temperature of wind flow under varying thickness of the heat insulation layer, exothermic water influx, seasonal working conditions, and other factors. This study examined the heat transfer changes in the shaft space before and after the application of foam concrete in order to verify the practicality of foam concrete for heat insulation in shaft engineering. The results of this study have significant practical implications for preventing and controlling heat hazards in hot shafts.

2. RAW MATERIALS AND EXPERIMENT METHODS

2.1. Raw Materials. Foam concrete, an effective thermal insulation material for underground tunnels, is primarily composed of portland cement, fly ash, aggregate, redispersible latex powder, polypropylene fibers, an accelerator, and a composite foaming agent. Foam concrete is a prime choice for the coating material of deep tunnels due to its noncombustibility and inorganic composition. The relevant parameters and selection criteria are illustrated in Table 1. Prior to conducting the experiment, the chemical composition of portland cement is analyzed using an X-ray diffractometer. The chemical composition is primarily composed of SiO_2, CaO, Al_2O, etc., with corresponding mass fractions as listed in Table 2. Table 3

Table 2. Chemical Composition of Portland Cement

chemical composition	CaO	Al_2O_3	Fe_2O_3	SiO_2	MgO
wt/%	66.1	5.2	4.0	22.6	1.3

Table 3. Content of Each Raw Material of the Compound Foaming Agent

material	synthetic surfactant	stabilizer	animal protein surfactant	tackifier
wt/%	60	3	36	1

displays the content of each raw material of the compound foaming agent. This physical foaming agent possesses high surface activity, which effectively reduces liquid surface tension. Double electron layers arrange themselves at the surface of the liquid film, shielding air and creating bubbles. Upon assessment, the foam's foaming factor can reach up to 30 times, exhibiting robust stability and resistance to defoaming.

https://doi.org/10.1021/acsomega.3c06929
ACS Omega 2023, 8, 48091−48103

2.2. Experimental Program. Based on the orthogonal experiment method, the compound experiments of foamed concrete with different compound ratios were designed, and the horizontal values of the four factors were determined by taking the amount of fly ash, redispersible latex powder, polypropylene fiber, and water−cement ratio as experimental factors, as shown in Table 4. The total amount of cementitious materials in the compound experiment is 2500 g. According to the selected level values of various factors, nine different reference groups can be obtained by an orthogonal experiment, and the specific values of each raw material in each reference group are determined, as shown in Table 5.

Table 4. Level Table of Each Factor

level	A fly ash	B latex powder	C polypropylene fibers	D water−cement ratio
1	25%	0.5%	0.2%	0.50
2	30%	1%	0.4%	0.55
3	35%	1.5%	0.6%	0.60

2.3. Preparation Process. The foamed concrete preparation process involves three main steps. First, foam was created using high-pressure air. The foaming agent and water were mixed in a ratio of 1:15, and the foaming agent diluent was thoroughly stirred with high-pressure gas from an air compressor. The foaming agent had exceptional surface activity, reducing liquid surface tension and producing a rich, stable foam.

Second, the remaining raw materials (such as cement, fly ash, polypropylene fiber, accelerator, redispersible latex powder, etc.) were weighed using an electronic balance, transferred into a blender, and thoroughly mixed beforehand. Next, a specific amount of water was added, and the ingredients were mixed for 1−2 min until a homogeneous cement-based slurry was attained.

Finally, the preprepared foam was added to the cement slurry, along with a specific amount of hydrogen peroxide solution. After the mixture was stirred thoroughly, it was poured into the triplex steel test mold and left to precure for 1−2 days. Following this, the product was removed from the mold and placed in a standard cement concrete curing box for 28 days to achieve the final result. The process of case preparation is shown in Figure 1.

3. DETERMINATION OF PERFORMANCE PARAMETERS OF THERMAL INSULATION MATERIALS

3.1. Analysis of Macroscopic Performance Measurement. According to the JG/T 266-2011 foam concrete standard specifications,[42] the specimens were tested for dry density, water absorption, thermal conductivity, and compressive strength using electronic balances, universal testing machines, thermal conductivity testers, electric drying oven, and other equipment. The test results are listed in Table 6.

An analysis of Table 6 reveals that the thermal conductivity of insulating foam concrete ranges from 0.194 to 0.270 W/(mK), while the compressive strength varies between 1.61 and 2.58 MPa across different compounding schemes. Given the high-temperature conditions in the deep shaft, the insulation material applied to its inner wall must possess properties of low thermal conductivity and high compressive strength. After evaluating each specimen's performance parameters, it was determined that case 4 exhibited the lowest thermal conductivity of 0.194W/(mK) and the highest compressive strength of 2.58 MPa.

3.2. Analysis of Fine Structure Determination. Using a scanning electron microscope at magnifications of 2000×, the internal microstructures of case 4, case 6, case 7, and case 9 were imaged using a high-resolution camera, as depicted in Figure 2.

Figure 2 depicts the material's structural characteristics and internal surface. As shown in Figure 2a captured by a scanning electron microscope, case 4's internal surface appears flat, with dense and uniform distribution of micropores. Additionally, there were visible small-sized holes that highlight the tightly bonded nature of the cement mortar material. Hence, the microstructure indicated that the configuration of case 4 is optimal. Upon observation of Figure 2b, it was apparent that the internal surface of case 6 was uneven and elevated. It was also evident that the cement mortar material exhibits numerous cracks within, and the bonding effect is general. In Figure 2c, the inner surface of case 7 is rough and has many protrusions. Under a magnification of 2000×, it can be clearly seen that the cement mortar material has cracks and holes. By observing Figure 2d, it can be seen that the inner surface of case 9 is relatively flat, and it can be seen clearly that the holes in the cement mortar material are evenly distributed, and there are many holes with smaller sizes. Through the comparison of these four groups of cases, it can be concluded that the inner surface of case 4 is relatively flat, with dense and evenly distributed micropores, and there are many small holes, which clearly show that the cement mortar material is closely bonded.

4. ANALYSIS OF PORE STRUCTURE AND THERMAL RESISTANCE OF FOAM CONCRETE TEST BLOCKS

4.1. Pore Structure Treatment Method and Analysis. Foam concrete is a lightweight and low thermal conductivity material that offers advantages over traditional concrete, including its low density and thermal conductivity. The interior of the foam concrete contains a significant number of bubbles that are introduced through mechanical mixing with a foam agent. This results in the formation of a large number of pores

Table 5. Specific Values of Components in Nine Different Reference Groups

number	portland cement/g	fly ash/g	aggregate/g	latex powder/g	polypropylene fibers/g	water/g	accelerator/g	foam admixture/g	H_2O_2/g
SY-1	1875	625	500	12.5	5.0	1250	37.5	500	100
SY-2	1875	625	500	25.0	10.0	1375	37.5	500	100
SY-3	1875	625	500	37.5	15.0	1500	37.5	500	100
SY-4	1750	750	500	12.5	10.0	1500	37.5	500	100
SY-5	1750	750	500	25.0	15.0	1250	37.5	500	100
SY-6	1750	750	500	37.5	5.0	1375	37.5	500	100
SY-7	1625	875	500	12.5	15.0	1375	37.5	500	100
SY-8	1625	875	500	25.0	5.0	1500	37.5	500	100
SY-9	1625	875	500	37.5	10.0	1250	37.5	500	100

https://doi.org/10.1021/acsomega.3c06929
ACS Omega 2023, 8, 48091−48103

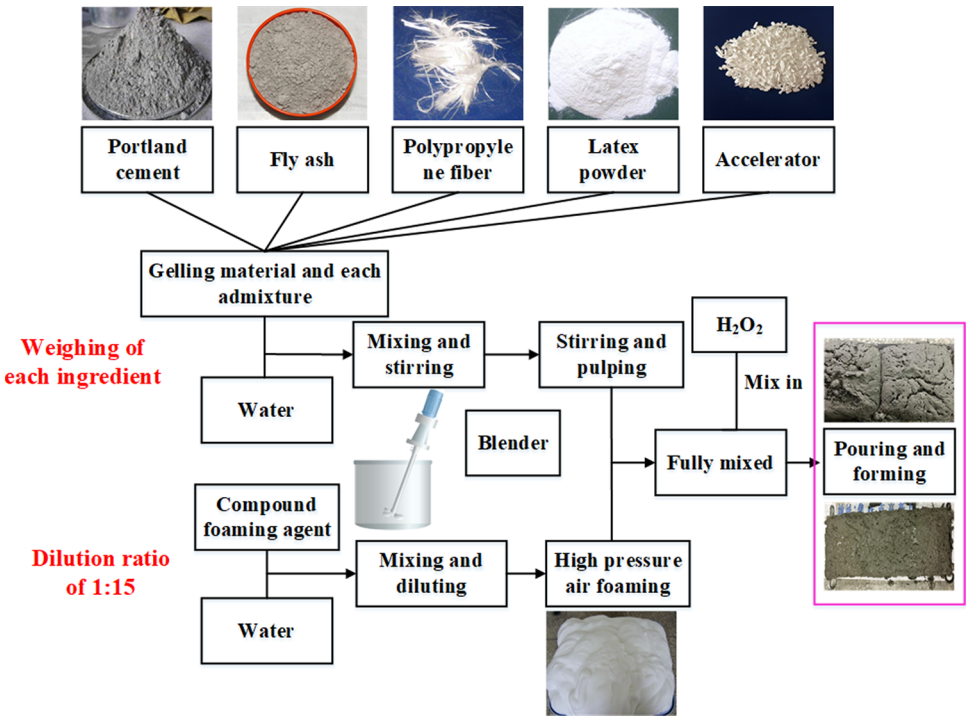

Figure 1. Process of case preparation.

Table 6. Main Performance Index Data for Each Experimental Working Condition

case number	dry density, kg/m^3	water absorption rate, %	compressive strength, MPa	thermal conductivity, W/(mK)
SY-1	674.0	32.5	2.51	0.270
SY-2	779.5	39.3	2.09	0.243
SY-3	646.6	46.5	1.61	0.214
SY-4	602.7	51.6	2.58	0.194
SY-5	673.2	46.1	2.00	0.216
SY-6	559.2	46.2	2.22	0.215
SY-7	576.8	48.9	2.34	0.204
SY-8	594.3	41.6	2.19	0.234
SY-9	665.6	39.7	2.41	0.241

with a more uniform and porous structure. The pores contain air, which acts as an effective adiabatic medium to block external heat transfer, thereby enhancing the thermal insulation properties of the foam concrete.

Figure 3 displays the concrete surface subsequent to cutting of the concrete sample. The sample, which was dried and cured, was cut parallel to the pouring surface. After removing surface powder, the morphology of the sample's surface was photographed. In order to reduce the influence of formwork and plastering methods on concrete surface pores, we have taken the following measures: carefully select the formwork with smooth surface and no obvious burrs or defects. The construction operation is fine, so as to ensure that the surface is trimmed in time to avoid uneven force, which leads to poor concrete compactness and large pores. Before plastering, the concrete surface should be kept dry, and the mixture ratio and water content of cement mortar should be controlled to achieve consistent scraping in batches and strengthen the maintenance management, keep the concrete surface moist in time, so as to avoid cracks or larger pores.

The pictures captured were black and red binarization treatments using Image-Pro Plus 6.0 software (shown in Figure 3, where the red area represents the pore and the black area is the slurry) to observe the distribution of the pixel size of the pores inside each group of specimens. The quantity and structure of pores on the surface of the cases with varying fit ratios varied. As depicted in Figure 3, case 4 displayed the greatest number of surface micropores. Additionally, in accordance with Figure 3, the internal surface of case 4 was densely packed with micropores, while case 6 exhibited sparser porosity with fewer pores in comparison with the other cases. As a result, it can be concluded that case 4 had a more evenly distributed structure and contained larger pores on the interior surface.

4.2. Correlation Analysis of Pore Structure and Thermal Insulation. As the internal pores of foam concrete contain an excellent adiabatic medium—air, it effectively blocks heat transfer. Therefore, the thermal conductivity of foam concrete is closely related to the number of pores. This correlation enables a more quantitative analysis of how the structure of the pores affects the thermal insulation of foam concrete. The surface pore structure of foam concrete specimens was analyzed quantitatively using Image-Pro Plus 6.0 software. Pores with diameter sizes ranging from 0.5 to 1 mm, 1−2 mm, and 2−3 mm were identified and counted. From a literature review and actual analysis, it was determined that bubble pore sizes of no more than 2 mm are suitable for achieving optimal dry density and thermal conductivity. Therefore, the number of pores with diameters in the range of 1−2 mm was selected as the primary measurement for correlation analysis with thermal conductivity. Table 7 illustrates the number of 1−2 mm pores for each group of cases. Combining these results with thermal conductivity values for each group from Table 6, the relationship between thermal conductivity and the number of 1−2 mm pores is depicted in Figure 4.

Upon observation of Figure 4, it is evident that there exists a correlation between the quantity of stomatal apertures within

https://doi.org/10.1021/acsomega.3c06929
ACS Omega 2023, 8, 48091−48103

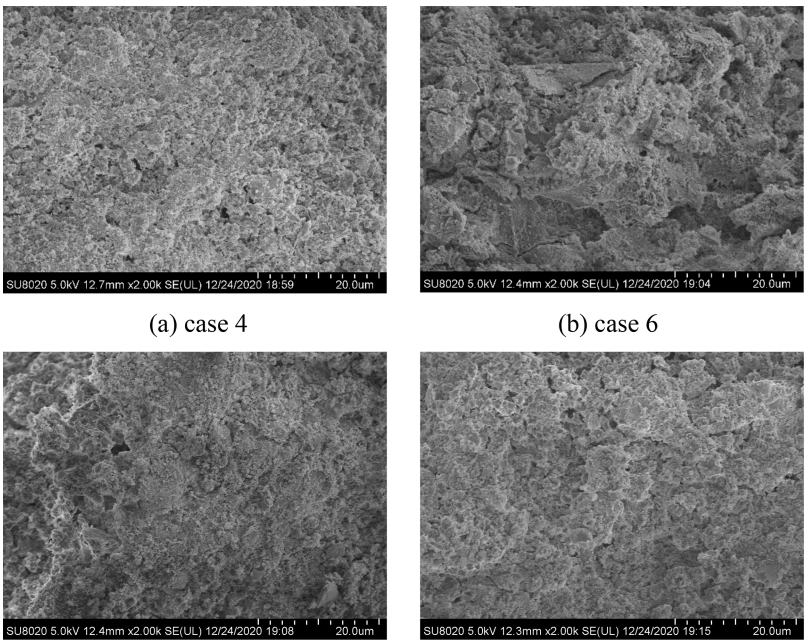

(a) case 4 (b) case 6

(c) case 7 (d) case 9

Figure 2. SEM images of (a) case 4, (b) case 6, (c) case 7, and (d) case 9.

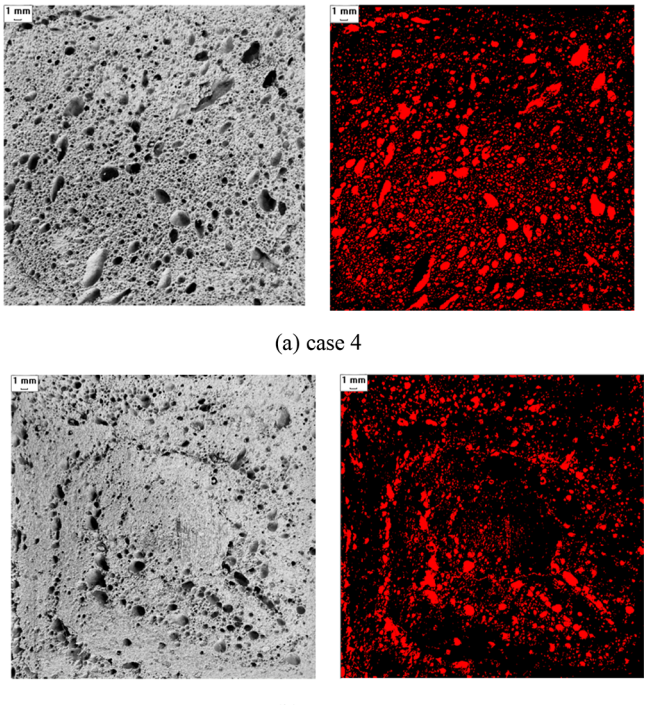

(a) case 4

(b) case 6

Figure 3. Internal surface diagram and software processing diagram of (a) case 4 and (b) case 6.

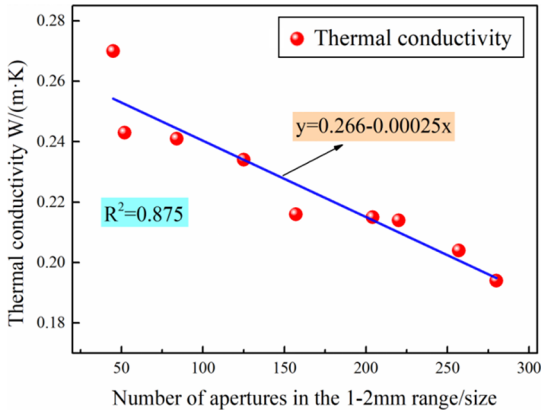

Figure 4. Relationship between the number of pores and thermal conductivity.

the 1−2 mm range and thermal conductivity. A linear fit of both variables reveals that the overall thermal conductivity for each condition decreases proportionally with an increase in pore diameters within the 1−2 mm range. Specifically, the linear equation is $y = 0.266 - 0.00025 \times x$, with a correlation coefficient of $R^2 = 0.875$, exceeding the minimum threshold of 0.8. Notably, the slope of the equation is negative, indicating a strong negative correlation between the two variables. This is mainly because with the increase in the number of stomata pore size in 1−2 mm, the air contained in the stomata is also a good insulation medium, which can block the transfer of certain heat.

4.3. Heat Transfer Path and Thermal Resistance Analysis Based on COMSOL. The heat barrier effect of the foam concrete can be categorized into two primary aspects. On the one hand, the porous structure within foam concrete impedes heat transfer from one side to the other. When heat encounters the bubble wall, the gas−liquid interface adhesion

Table 7. Number of 1−2 mm Pores for Each Group of Cases

case	SY-1	SY-2	SY-3	SY-4	SY-5	SY-6	SY-7	SY-8	SY-9
1−2 mm number of pores/size	45	52	220	280	157	204	257	125	84

https://doi.org/10.1021/acsomega.3c06929
ACS Omega 2023, 8, 48091−48103

and force within the bubble prevent further transfer. In other words, due to the varying thermal resistance of the slurry and bubble walls, portions of the heat can bypass the bubbles, further lengthening the heat transfer path. On the other hand, there is a significant number of free gas molecules in the pores of foam concrete. As gas phase heat transfer occurs through collisions between gas molecules, such collisions accelerate the transfer of heat while disrupting the original heat conduction of the solid phase matrix. As a result, the gas molecules become agitated, and the heat transfer process is weakened. This leads to a greater dissipation of heat as it passes through the bubbles.

To better visualize and analyze the heat transfer pathway inside the foam concrete sample and to determine the thermal resistance of different compound configurations, we conducted a simulation using case 4 as the model. The size and quantity of pores are determined through imaging techniques using a Canon EOS 5DS SLR camera, while Image-Pro Plus 6.0 software is used to observe the distribution of pore sizes in each sample group. Using COMSOL simulation software, we created a two-dimensional model of the instantaneous heat transfer within the pore structure of the foam concrete. (For the sake of clarity, we designated circles of varying diameters to represent the pores within the foam concrete.). The foam concrete section in the model had a side length of 100 mm × 100 mm, with a thermal conductivity of 0.194 W/(mK) and a dry density of 602.7 kg/m^3. The thermal conductivity of the air bubbles present in the simulation was set to 0.023 W/(mK), with a specific heat capacity of 1005 J/(kg·°C) and density of 1.18 kg/m^3. The initial temperature at the left boundary of the model was set to 40 °C, while the right boundary temperature was 20 °C. The right and left boundaries exchanged heat through convective heat flux, with a heat transfer coefficient of 0.1 W/(m^2·K). The rest of the boundary was insulated, and the external ambient temperature was maintained at 20 °C. Under the given conditions, the grid is divided into a free-form triangle grid, while the foam is further subdivided into finer grids and the pores are divided into ultrafine grids, as demonstrated in Figure 5. Figure 6 shows the heat transfer process of foam concrete with a density of 602.7 kg/m^3 at different moments.

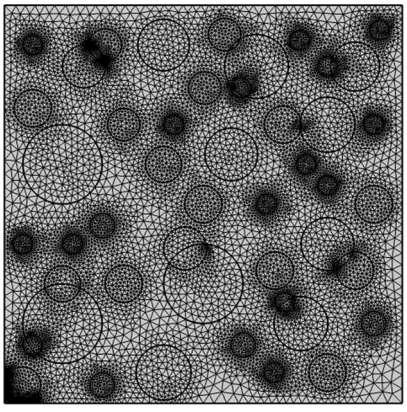

Figure 5. Gridding diagram of foam concrete.

Upon examination of Figure 6, it is evident that as heat transfer time increases, heat is continuously transferred from areas of high temperature to those of lower temperature. Specifically, the transfer occurs from the left side of the foam concrete section to the right side. The black line in the figure depicts the path of heat transfer within the foam concrete, with the direction of the arrow indicating the direction of heat transfer. Multiple routes of heat transfer are present within the foam concrete, with the heat flow line assuming a concave or convex form when encountering bubbles. These routes can be categorized into two types: the first being the forward transfer that avoids bubbles (i.e., slurry) and the second being the transfer through bubbles, which corresponds to the heat-blocking effect that foam concrete has.

5. ENGINEERING SIMULATION AND ANALYSIS OF THERMAL INSULATION EFFECT

5.1. Engineering Simulation Objects and Basic Parameters. With the help of Ansys Fluent software, a physical model of the tunneling roadway solely made of coal had been constructed. The model comprises the roadway and the encompassing rock, and its cross-section can be visualized in Figure 7. The model roadway had a length of 300 m, and Table 8 shows the situation of its roof and floor. The roof and floor were made of limestone, while the sidewall consists of a coal seam. To provide optimal heat insulation, we applied a new material to the internal sidewall and roof of the roadway. The tunnel was a newly dug tunnel; the initial temperature of the surrounding rock was set to the original rock temperature of 39.7 °C; and the internal diameter of the surrounding rock was 40 m.

The inlet for the model was established as a velocity inlet at the section where air exits the duct tunnel. The exit of the duct tunnel was defined as the entrance boundary of the model and set to have a pressure exit boundary condition. The dry bulb temperature of the inlet air in winter was 19.8 °C, the wet bulb temperature was 19.4 °C, and the wind speed was 1.683 m/s; the dry bulb temperature of the inlet air in spring and autumn was 25.2 °C, the wet bulb temperature was 24.6 °C, and the wind speed was 0.9 m/s; the dry bulb temperature of the inlet air in summer was 34.7 °C, the wet bulb temperature was 33.9 °C, and the wind speed was 0.9 m/s. The alleyway was not equipped with drains, and the heat emitted by the gushing water to the alleyway was taken as 126 kW, 105 kW, and 42 kW in winter, spring and autumn, and summer, respectively, which were converted into the internal heat source of fluid area, 30, 25, and 10 W/m^3, respectively. The physical properties of air were determined based on the temperature and humidity of the inlet airflow, while the key performance parameters of other materials are presented in Table 9.

Ansys Meshing was utilized for the meshing process, resulting in 835,400 mesh cells. The Fluent software was employed to conduct the calculations using the $k-\varepsilon$ model for the turbulence model and activating the energy model. For heat transfer analysis of the insulation layer, the shell conduction model was utilized. In the solver parameters, the pressure−velocity coupling method was set to SMPLEC.

5.2. Systematic Analysis of Engineering Simulation Results. *5.2.1. Analysis of Temperature Changes in the Tunnel.* Figures 8 and 9 show the temperature distribution of the cross-sectional plane (z = 150 m) and axial plane (x = 0 m) of the model, respectively, under varying ventilation durations with 100 mm insulation thickness during winter conditions.

As shown in Figure 8, it is evident that as ventilation time increases, the temperature distribution across the cross-section of the tunnel enclosure undergoes continuous changes. Additionally, the radius of the regulated heat circle gradually expands. This is primarily due to the disturbance of the original thermal balance of the rock at the periphery of the roadway during excavation and ventilation. As a result, the temperature

https://doi.org/10.1021/acsomega.3c06929
ACS Omega 2023, 8, 48091−48103

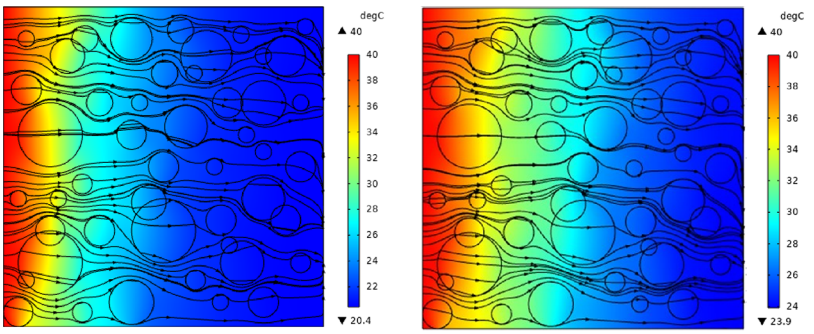

(a) The heat transfer time is 40mins (b) The heat transfer time is 120mins

Figure 6. Teat transfer process at different moments. (a) Heat transfer time is 40 min. (b) Heat transfer time is 120 min.

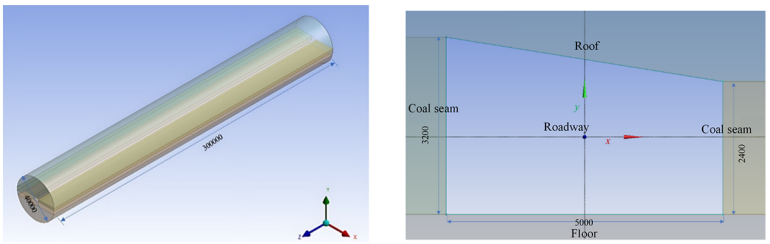

(a) Physical model of all-coal heading roadway (b) Cross-section of a physical model of an all-coal roadway

Figure 7. Physical modeling of an all-coal roadway (unit: mm). (a) Physical model of all-coal heading roadway. (b) Cross-section of a physical model of an all-coal roadway.

Table 8. Table of Roof and Floor of the All-Coal Tunneling Roadway

roof and floor name		rock category	thickness
roof	immediate roof	limestone	5.39 m
	false roof	no	no
floor	direct floor	sandy mudstone	4.03 m
	basic floor	limestone	11.6 m

Table 9. Material Parameter Table of the All-Coal Tunneling Roadway

rock properties	density, m^3/kg	specific heat capacity, J/(kg·K)	thermal conductivity, W/mK
sandy mudstone	2655	932.14	2.00
limestone	2679	907.06	2.28
anthracite coal	1400	1130	0.24
thermal insulation	602.7	840	0.194

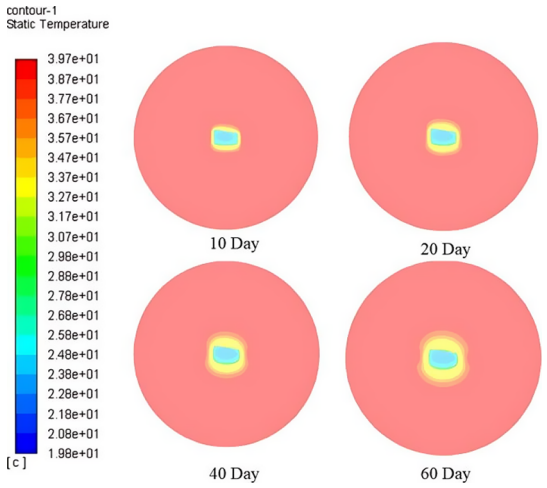

Figure 8. Temperature distribution at the cross-section of surrounding rock (z = 150 m).

difference between the airflow and the surrounding rock drives continuous heat transfer from the rock to the airflow. Subsequently, the airflow carries away the accumulated heat from the surrounding rock, resulting in a steady decrease in its temperature. As ventilation progresses, the cooling reduction zone extends further into the rock, and the radius of the heat transfer zone gradually increases. Moreover, due to the lower thermal conductivity of bituminous coal compared to limestone, the affected area of the temperature at the sidewall caused by bituminous coal is smaller than that at the vault of limestone. From Figure 9, it can be concluded that as the ventilation time keeps increasing, the wind flow continuously absorbs the heat released from the surrounding rock and gushing water during the flow in the tunnel, resulting in a gradual increase in the temperature of the wind flow, which in turn eventually reaches the maximum average temperature at the model exit (entrance of the dug tunnel).

5.2.2. Analysis of Heat Dissipation in the Tunnel Envelope and Airflow Outlet Temperature. Figures 10 and 11 depict the pattern of heat dissipation from the adjacent rock to the wind flow and the outlet temperature of the tunnel wind flow across varying insulation thicknesses (0−400 mm) during the winter, correspondingly.

From Figures 10 and 11, it is clear that the trend of heat dissipation from the surrounding rock to the wind flow and the average temperature of the wind flow outlet in the roadway, during different thicknesses of insulation layers in wintertime, are similar for the all-coal tunneling roadway. Both display a gradual decrease as the ventilation time increases, with the most notable reduction in heat dissipation and wind flow outlet

https://doi.org/10.1021/acsomega.3c06929
ACS Omega 2023, 8, 48091−48103

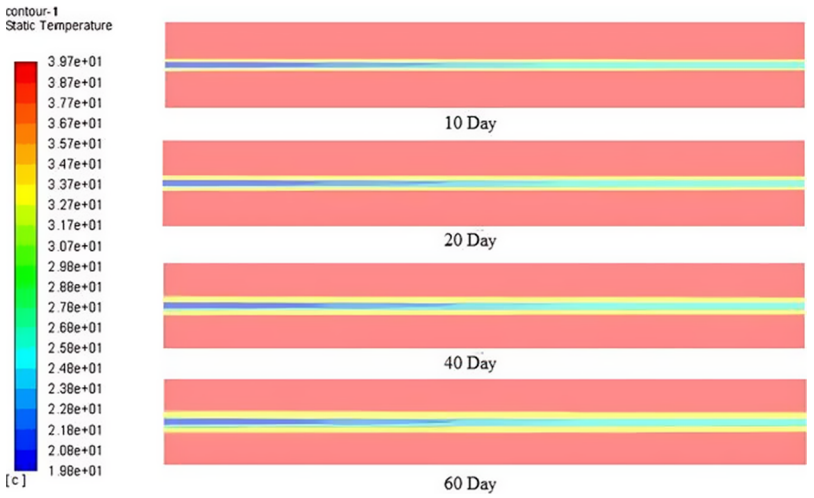

Figure 9. Temperature distribution at the axial section of surrounding rock (x = 0 m).

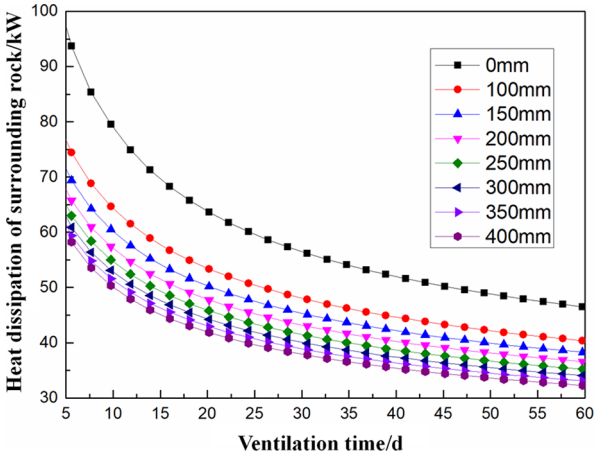

Figure 10. Heat dissipation of surrounding rock to airflow under different thicknesses of the thermal insulation layer (winter).

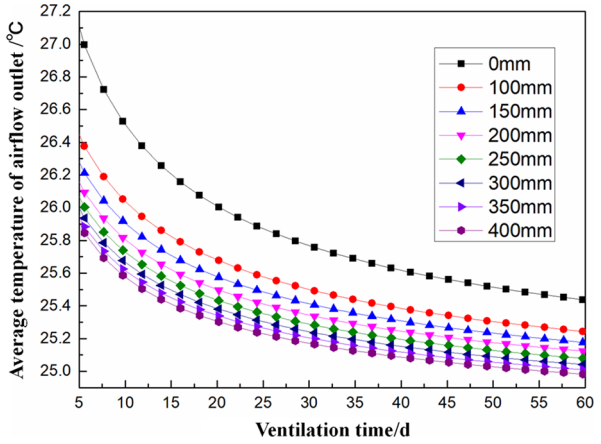

Figure 11. Average temperature of roadway airflow outlet under different thicknesses of the thermal insulation layer (winter).

temperature occurring between 5 and 20 days of ventilation. The decrease in ventilation time results in a continuous rise in temperature in the rock wall of the surrounding tunnel. This in turn reduces the temperature difference between the wind flow and the rock wall, leading to a decline in heat transfer and ultimately causing the tunnel wind flow outlet temperature to plummet. Compared to unsprayed insulation, the heat dissipation from the surrounding rock to the wind flow and the average temperature at the outlet are reduced to less than 80 kW and 26.5 °C, respectively, during initial ventilation. Additionally, when ventilation is terminated, heat dissipation and the average temperature at the outlet fall to less than 46 kW and 25.3 °C, respectively. With a 400 mm thickness of sprayed insulation, surrounding rock heat dissipation to wind flow and the average temperature at the tunnel's outlet can be reduced to below 33 kW and 25 °C, respectively. The main reason for this is that increasing the thickness of the thermal insulation layer can reduce the heat transfer from the tunnel's surrounding rock to the airflow when the ventilation time is the same. This reduction will result in a decrease in the average temperature of the wind flow outlet in the tunnel, as well as a decrease in the average temperature of the wind flow within the tunnel. Therefore, the developed shaft insulation material provides superior insulation effectiveness.

5.2.3. Analysis of the Rate of Reduction of Heat Dissipation and Gushing Water Discharge in the Roadway Enclosure. The insulating properties of the insulating layer are assessed by measuring the reduction rate of heat dissipation from the surrounding rock:

$$\eta = \frac{Q - Q_i}{Q} \times 100\% \quad (1)$$

where η is the reduction rate of heat dissipation of surrounding rock, Q is the heat dissipation of surrounding rock to wind flow when no insulation layer is applied, and Q_i is the heat dissipation of surrounding rock to wind flow when different thickness of insulation layer is applied.

The rate of heat dissipation reduction in the surrounding rock is calculated by using numerical methods for different insulation thicknesses, as shown in Figure 10. Figure 12 illustrates the changes in the heat dissipation reduction rate of the surrounding rock during winter for different insulation thicknesses and ventilation durations.

As presented in Figure 12, it is evident that the reduction rate of heat dissipation in the surrounding rock of the all-coal tunneling tunnel decreases with an increase in the ventilation time for the same thickness of the thermal insulation layer. The magnitude of this decrease gradually diminishes. Additionally, the reduction rate of heat dissipation in the surrounding rock

https://doi.org/10.1021/acsomega.3c06929
ACS Omega 2023, 8, 48091−48103

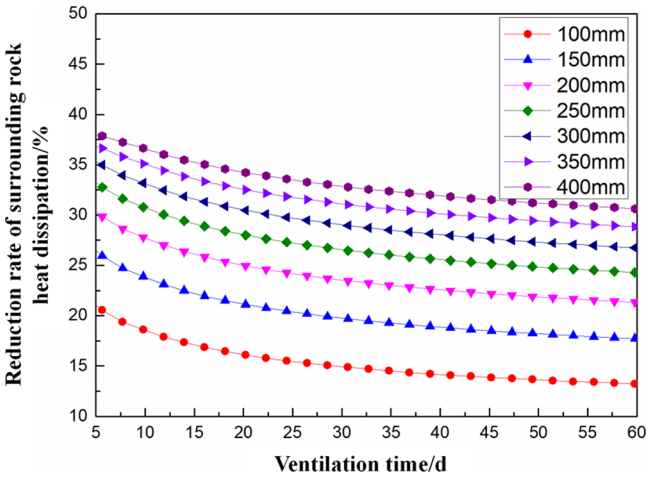

Figure 12. Reduction rate of surrounding rock heat dissipation under different thicknesses of the thermal insulation layer (winter).

increases as the insulation layer thickness increases for the same ventilation time. The magnitude of this increase gradually decreases as well. Among them, when the ventilation period is 60 days, the presence of insulation layers with thicknesses of 300 and 400 mm can reduce the heat dissipation of surrounding rock by 26.7 and 31.8%, respectively, compared with scenarios without insulation layers. This finding suggests that insulation layers can effectively mitigate heat transfer from surrounding rocks to the roadway. In addition, greater thickness of the insulation layer leads to a greater reduction in heat transfer from surrounding rocks to the roadway.

Based on the calculation above, it can be observed that the heat dissipation of the surge water is higher than that of the surrounding rock. For example, when the insulation layer is 300 mm, the surge water dissipates 126 kW, while the surrounding rock only dissipates 34.0 kW after a ventilation period of 60 days. In order to analyze the influence of the surge water dissipation on the performance of the insulation layer, Figure 13a,b displays the average temperature of the surrounding rock and the wind flow heat dissipation at the tunnel outlet under different surge water dissipation, respectively, for an insulation layer thickness of 300 mm.

Based on Figure 13a,b, it is evident that the heat dissipation of the surrounding rock and the average air outlet temperature exhibit similar variation trends under different water inflows and heat releases. Both show a decreasing trend as ventilation time increases, with the most significant reduction in heat dissipation occurring between 5 and 20 days of ventilation. As the water inflow heat increases, the heat dissipation of the surrounding rock and the average temperature of the air outlet gradually decrease, while the ventilation time remains constant. Specifically, when the water inflow heat reaches 126 kW and the ventilation period is 60 days, the minimum heat dissipation of the surrounding rock can be reduced to 34 kW, and the air outlet temperature can be lowered to 21.3 °C. The reason for this is mainly due to the escalating heat release caused by the influx of water. As a result, more heat is released to the roadway, leading to a continuous rise in the outlet temperature of the airflow in the roadway. As a result, the average temperature of the airflow in the roadway gradually increases, causing thermal stability and environmental deterioration. However, this reduces the temperature difference in heat transfer between the roadway and the surrounding rock, resulting in reduced heat dissipation from the surrounding rock to the roadway in proportion to the heat released by the water influx.

Figure 14 shows the rate of reduction in the heat dissipation of the surrounding rock under four types of water inrush heat release. Despite the decrease in heat dissipation of the surrounding rock with an increase in water inrush heat release, the reduction in heat dissipation rate of the surrounding rock remains consistent with different ventilation times, as compared to that without a thermal insulation layer.

5.2.4. Analysis of Thermal Insulation Effect of the Thermal Insulation Layer in Different Seasons. Figures 15 and 16 show the dissipation of heat from the surrounding rock, the outlet temperature of the airflow, and the decrease in the dissipation rate of heat from the surrounding rock across different insulation thicknesses during spring, autumn, and summer, respectively.

Compared with the winter working conditions depicted in Figures 10−12, it is evident that the heat dissipation of the surrounding rock with varying insulation thickness, the outlet

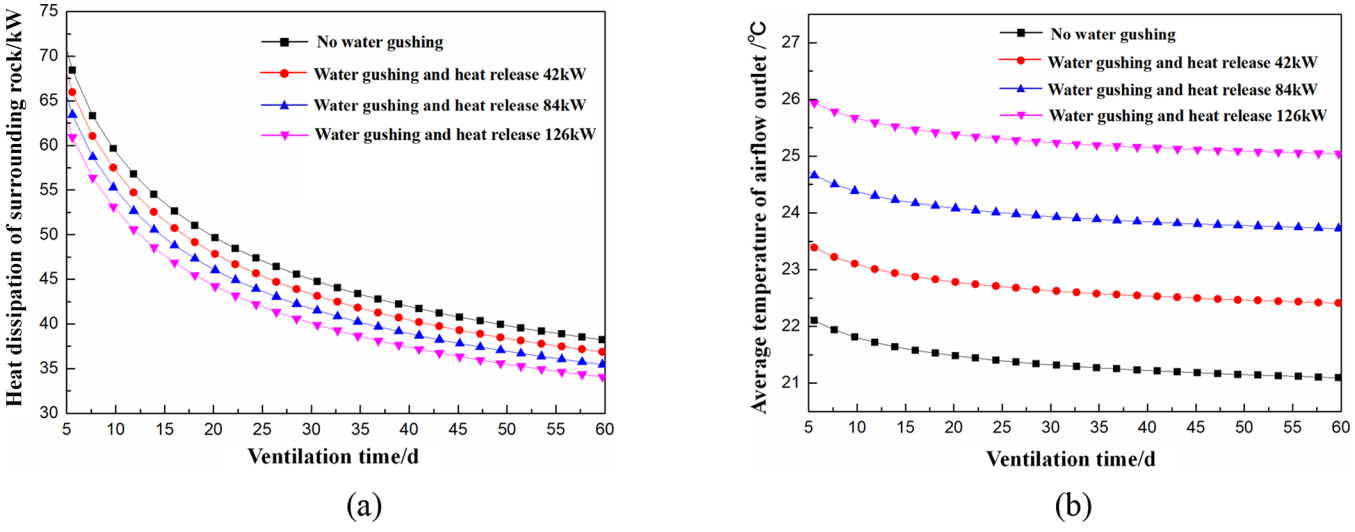

Figure 13. Heat dissipation (a) of surrounding rock to airflow and average temperature of airflow outlet (b) under different water gushing heats of all-coal tunneling roadway (winter).

https://doi.org/10.1021/acsomega.3c06929
ACS Omega 2023, 8, 48091−48103

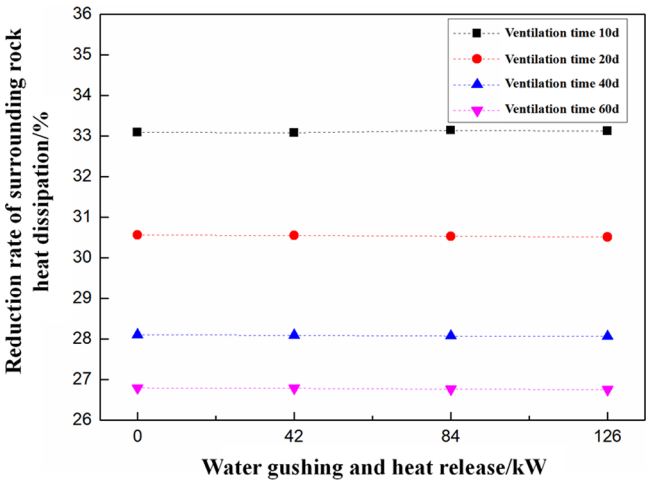

Figure 14. Reduction rate of surrounding rock heat dissipation under different water gushing conditions and heat release (winter).

temperature of the airflow, and the reduction rate of the heat dissipation of the surrounding rock exhibit similar trends during spring, autumn, and summer working conditions. Specifically, they gradually decrease with an increased ventilation time. When the seasonal working conditions and ventilation time are the same, the heat dissipation of the surrounding rock and the outlet temperature of airflow decrease with the increase of insulation layer thickness. The reduction rate of heat dissipation of the surrounding rock gradually increases with the increase of insulation thickness.

In order to gain a clearer understanding and conduct a thorough study of the impact of seasonal working conditions on the performance of the thermal insulation layer, an analysis and comparison of heat dissipation and air outlet temperature of the surrounding rock with a 300 mm thermal insulation layer was carried out for 60 days across various seasons. The results were then compared with those without the thermal insulation layer, as outlined in Table 10.

Based on the findings in Table 10, it can be inferred that the heat dissipation of the surrounding rock and the temperature of the airflow exiting the roadway with a 300 mm thermal insulation layer are remarkably lower than those without insulation.

This provides evidence that the thermal insulation material used in the layer has an effective thermal insulation capacity. Due to the higher air temperature in the tunnel during summer compared to winter, spring, and autumn, and the small heat transfer temperature difference between the tunnel and surrounding rock, which is only 0.09 °C, the dissipation of heat from the surrounding rock is reduced. However, after the installation of a thermal insulation layer, the reduction in the

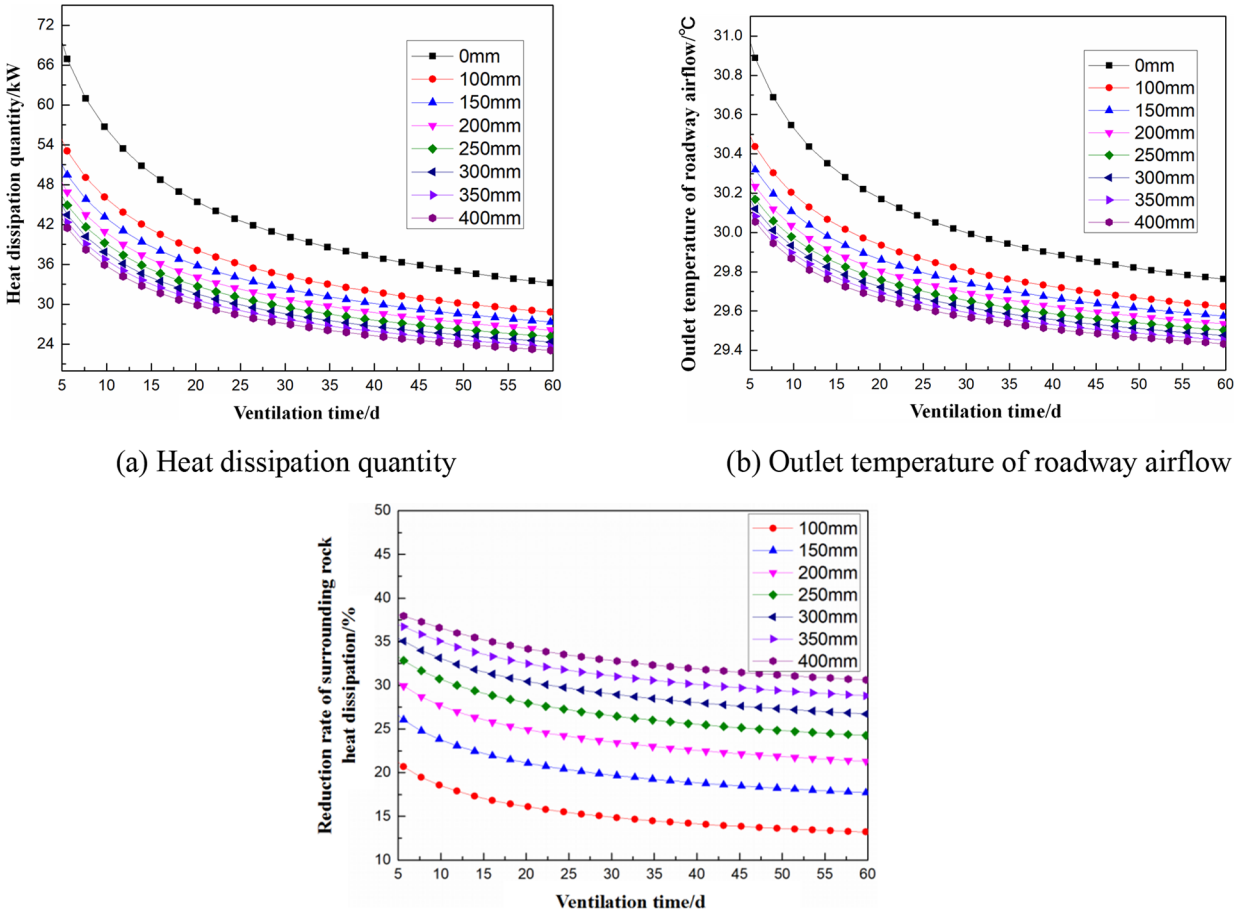

(a) Heat dissipation quantity

(b) Outlet temperature of roadway airflow

(c) Reduction rate of surrounding rock heat dissipation

Figure 15. Change of parameters under different insulation thicknesses (spring and autumn). (a) Heat dissipation quantity. (b) Outlet temperature of roadway airflow. (c) Reduction rate of surrounding rock heat dissipation.

https://doi.org/10.1021/acsomega.3c06929
ACS Omega 2023, 8, 48091−48103

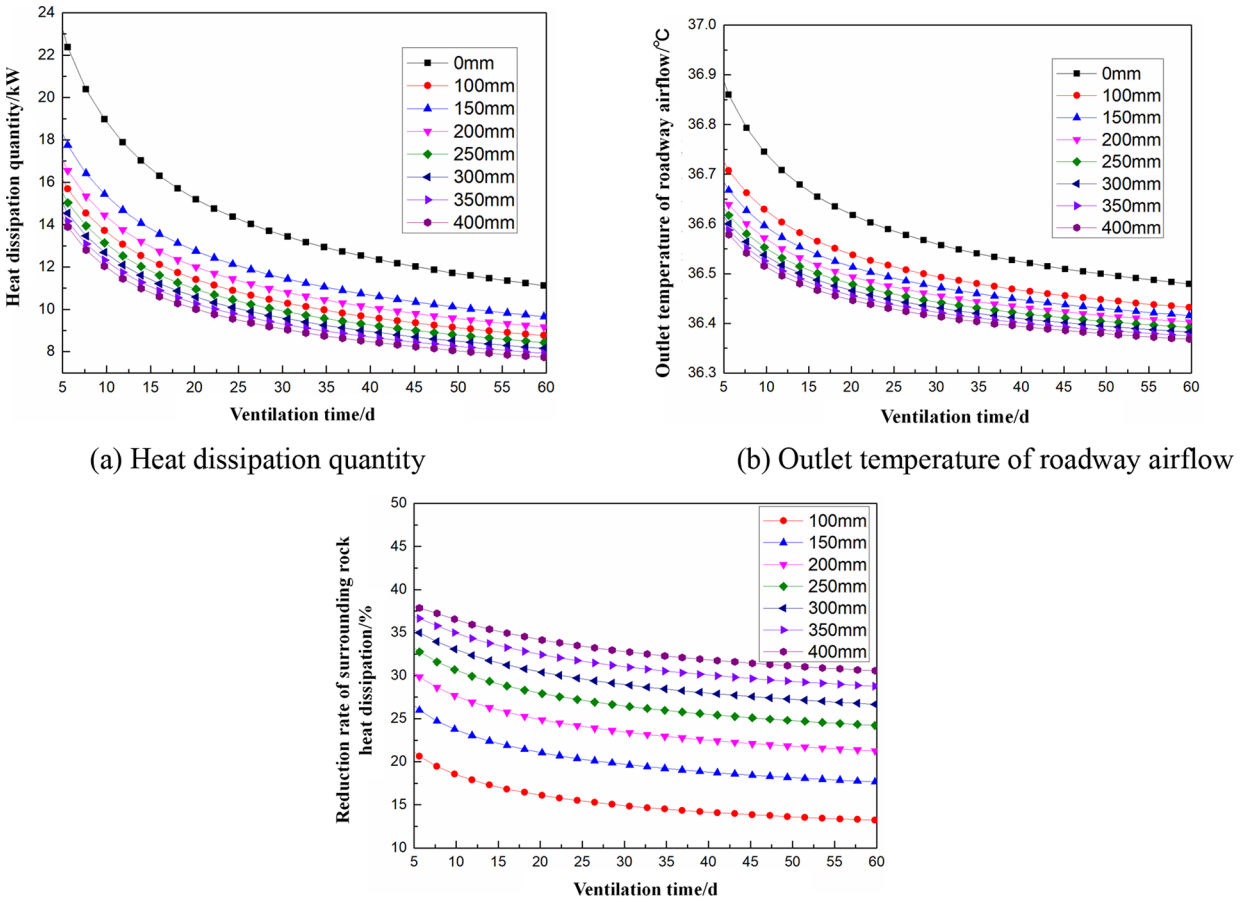

Figure 16. Change of parameters under different insulation thickness (summer). (a) Heat dissipation quantity. (b) Outlet temperature of roadway airflow. (c) Reduction rate of surrounding rock heat dissipation.

Table 10. Main Performance of the Thermal Insulation Layer in the All-Coal Tunneling Roadway in Different Seasons (Ventilation Time 60 d)

	heat dissipation of the surrounding rock (kW)		temperature of the airflow exiting the roadway (°C)		thermal insulation effect		
season	no thermal insulation layer	300 mm thermal insulation layer	no thermal insulation layer	300 mm thermal insulation layer	reduction of surrounding rock heat dissipation (kW)	reduction rate of surrounding rock heat dissipation (%)	temperature (°C)
winter	46.48	34.05	25.43	25.05	12.43	26.74	0.38
spring and autumn	33.17	24.31	29.78	29.5	8.86	26.72	0.28
summer	11.12	8.15	36.47	36.38	2.97	26.68	0.09

heat dissipation from the surrounding rock will be lessened. However, in all seasons, the heat dissipation reduction rate of the surrounding rock with a thermal insulation layer is almost equivalent to that without a thermal insulation layer at about 26.7%. This is mainly due to influential parameters, such as air temperature, wind speed, and water inflow heat release, while the heat dissipation reduction rate of the surrounding rock is mainly influenced by the thickness of the thermal insulation layer and ventilation time. The impact of the working conditions in all seasons is relatively minimal.

6. CONCLUSIONS

(1) Based on orthogonal experiments and microscopic morphology structure verification, the optimal ratio for the comprehensive performance of the new heat insulation material was determined through synergistic regulation using mechanical and chemical methods. The ideal ratio comprises 2500 g cementitious material, 30% of which is fly ash, and 0.5% and 0.4% redispersible latex powder and polypropylene fiber, respectively, doped with the cementitious material, and a water−cement ratio of 0.6.

(2) Using Image-Pro Plus 6.0 software to perform black and red binarization on captured photographs, we quantified the internal structure of foam concrete. The resulting fitting equation $y = 0.266 - 0.00025 \times x$ provided the thermal conductivity coefficient of the foam concrete and internal air pores. The equation had a correlation coefficient (R) of 0.935 and a negative slope, indicating a strong negative correlation between the two variables. This is mainly because an increase in the number of

https://doi.org/10.1021/acsomega.3c06929
ACS Omega 2023, 8, 48091−48103

stomatal pores with a diameter of 1−2 mm results in air becoming an excellent insulating medium that can inhibit heat transfer.

(3) To better visualize and analyze the thermal resistance of various foam concrete composites, we selected working condition 4 as our simulation subject and utilized the COMSOL simulation software to create a 2D model of the foam concrete. This allows us to intuitively demonstrate the path of heat transfer within the foam concrete and study its thermal characteristics.

(4) Based on the results of Fluent simulation experiments, the heat insulation layer of the new insulation material effectively minimizes heat dissipation from surrounding rock to the roadway, consequently reducing the temperature of wind flow in the tunnel. The rate of reduction in heat dissipation from the surrounding rock also increases with the heat insulation layer thickness, but the increase is not proportional.

(5) There are differences in the dissipation and reduction of heat from surrounding rock in roadway during different seasons; the main influencing factors are wind flow temperature, wind speed, heat release of gushing water, etc.

■ ASSOCIATED CONTENT

Data Availability Statement

All the data supporting the findings of our study are available in the article.

■ AUTHOR INFORMATION

Corresponding Author

Hailin Jia − *Collaborative Innovation Center of Coal Safety and Clean High Efficiency Utilization and State Key Laboratory Cultivation Base for Gas Geology and Gas Control, Henan Polytechnic University, Jiaozuo, Henan 454000, China;* orcid.org/0000-0003-0485-3302; Email: jiahailin@hpu.edu.cn

Authors

Qian Zou − *Collaborative Innovation Center of Coal Safety and Clean High Efficiency Utilization and State Key Laboratory Cultivation Base for Gas Geology and Gas Control, Henan Polytechnic University, Jiaozuo, Henan 454000, China;* orcid.org/0009-0008-4220-856X

Bo Cui − *Collaborative Innovation Center of Coal Safety and Clean High Efficiency Utilization and State Key Laboratory Cultivation Base for Gas Geology and Gas Control, Henan Polytechnic University, Jiaozuo, Henan 454000, China*

Jinxiang Zeng − *Collaborative Innovation Center of Coal Safety and Clean High Efficiency Utilization and State Key Laboratory Cultivation Base for Gas Geology and Gas Control, Henan Polytechnic University, Jiaozuo, Henan 454000, China*

Complete contact information is available at: https://pubs.acs.org/10.1021/acsomega.3c06929

Author Contributions

H.J.: conceptualization, methodology, investigation, writing—original draft, and funding acquisition. Q.Z.: investigation, computer simulation, data analysis, and writing—original draft. B.C.: investigation, laboratory test, data curation, and discussion. J.Z.: investigation, data curation, and discussion.

Notes

The authors declare no competing financial interest.

■ ACKNOWLEDGMENTS

This work was supported by the National Natural Science Foundation of China (52274185), the National Key Research and Development Program of China (2018YFC0807900), the Innovative Research Team of Ministry of Education of China (IRT_16R22), and Innovative Scientific Research Team of Henan Polytechnic University (T2021-4).

■ REFERENCES

(1) Luo, Z.; Li, R.; Wang, T.; Cheng, F.; Liu, Y.; Yu, Z.; Fan, S.; Zhu, X. Explosion pressure and flame characteristics of CO/CH4/air mixtures at elevated initial temperatures. *Journal Article* **2020**, *268*, No. 117377.

(2) Aydin, G.; Jang, H.; Topal, E. Energy consumption modeling using artificial neural networks: The case of the world's highest consumers. *Journal Article* **2016**, *11*, 212.

(3) Sun, B.; Zhang, P.; Wu, R.; Fu, M.; Ou, Y. Research on the overburden deformation and migration law in deep and extra-thick coal seam mining. *Journal Article* **2021**, *190*, No. 104337.

(4) Su, Z.; Jiang, Z.; Sun, Z. Study on the heat hazard of deep exploitation in high-temperature mines and its evaluation index. *Journal Article* **2009**, *1*, 414.

(5) Hancock, P. A. Specifying and Mitigating Thermal Stress Effects on Cognition During Personal Protective Equipment Use. *Journal Article* **2020**, *62*, 697.

(6) Roghanchi, P.; Kocsis, K. C. Challenges in Selecting an Appropriate Heat Stress Index to Protect Workers in Hot and Humid Underground Mines. *Journal Article* **2018**, *9*, 10.

(7) Zhongpeng, X. Distribution Law of High Temperature Mine's Thermal Environment Parameters and Study of Heat Damage's Causes. *Journal Article* **2012**, *43*, 588.

(8) He, M.; Cao, X.; Xie, Q.; Yang, J.; Qi, P.; Yang, Q.; Chen, X. Principles and technology for stepwise utilization of resources for mitigating deep mine heat hazards. *Journal Article* **2010**, *20*, 20.

(9) Xiaojie, Y.; Qiaoyun, H.; Jiewen, P.; Xiaowei, S.; Dinggui, H.; Chao, L. Progress of heat-hazard treatment in deep mines. *Journal Article* **2011**, *21*, 295.

(10) Guo, P.; Wang, Y.; Duan, M.; Pang, D.; Li, N. Research and application of methods for effectiveness evaluation of mine cooling system. *Journal Article* **2015**, *25*, 649.

(11) He, M. Application of HEMS cooling technology in deep mine heat hazard control. *Min. Sci. Technol.* **2009**, *19*, 269.

(12) van Staden, H. J.; van Rensburg, J. F.; Groenewald, H. J. Optimal use of mobile cooling units in a deep-level gold mine. *Journal Article* **2020**, *30*, 547.

(13) Feng, X.; Jia, Z.; Liang, H.; Wang, Z.; Wang, B.; Jiang, X.; Cao, H.; Sun, X. A full air cooling and heating system based on mine water source. *Journal Article* **2018**, *145*, 610.

(14) Guo, P.; Chen, C. Field experimental study on the cooling effect of mine cooling system acquiring cold source from return air. *Journal Article* **2013**, *23*, 453.

(15) Cong-guang, J.; Hui, Z.; Chun-sheng, H.; Gui-ping, L.; Wei, S.; Fang, Y. The Analysis of the Cooling System with Gas-Power-Generation and Waste Heat Refrigeration. *Journal Article* **2011**, *26*, 1011.

(16) Du Plessis, G. E.; Liebenberg, L.; Mathews, E. H. The use of variable speed drives for cost-effective energy savings in South African mine cooling systems. *Journal Article* **2013**, *111*, 16.

(17) du Plessis, G. E.; Liebenberg, L.; Mathews, E. H. Case study: The effects of a variable flow energy saving strategy on a deep-mine cooling system. *Journal Article* **2013**, *102*, 700.

(18) Faraz, A.; Omer, C.; Nesrin, A.; Sendogan, K. Optimal Charge Amount for Different Refrigerants in Air-to-Water Heat Pumps. *Iran. J. Sci. Technol., Trans. Mech. Eng.* **2016**, *40*, 325−335.

(19) Afshari, F.; Comakli, O.; Karagoz, S.; Zavaragh, H. G. A thermodynamic comparison between heat pump and refrigeration device using several refrigerants. *Journal Article* **2018**, *168*, 272.
(20) Wang, Y.; Hu, H.; Sun, X.; Zhang, Y.; Gong, D. Unified operation optimization model of integrated coal mine energy systems and its solutions based on autonomous intelligence. *Journal Article* **2022**, *328*, No. 120106.
(21) Wang, S.; Wang, W.; Shao, K.; Ding, W.; Cui, Z.; Shao, W.; Ji, W. Operation optimization of a refrigeration ventilation system for the deep metal mine. *Journal Article* **2023**, *44*, No. 102817.
(22) Hailin, J.; Haijun, X.; Mingsheng, G.; Wanli, Z.; Xiaoju, Z.; Minyuan, Z.; Shuijun, Y. Study on Combined System and Performance of the Thermal Insulation Material Applying to High Temperature Strata Tunnel in Deep Coalmine. *Mater. Rep.* **2022**, *36*, No. 21050031.
(23) Zhang, H.; Li, M.; Xiao, Y.; Han, X.; Liu, B.; Yang, W. Numerical study on interactions between climate conditions and diesel exhaust and optimization of auxiliary ventilation in underground mines. *Journal Article* **2023**, *37*, No. 101594.
(24) Amran, Y. H. M.; Farzadnia, N.; Abang Ali, A. A. Properties and applications of foamed concrete; a review. *Journal Article* **2015**, *101*, 990.
(25) Demirboğa, R.; Gül, R. The effects of expanded perlite aggregate, silica fume and fly ash on the thermal conductivity of lightweight concrete. *Journal Article* **2003**, *33*, 723.
(26) Xie, Y.; Li, J.; Lu, Z.; Jiang, J.; Niu, Y. Effects of bentonite slurry on air-void structure and properties of foamed concrete. *Journal Article* **2018**, *179*, 207.
(27) Kuzielová, E.; Pach, L.; Palou, M. Effect of activated foaming agent on the foam concrete properties. *Journal Article* **2016**, *125*, 998.
(28) Batool, F.; Bindiganavile, V. Air-void size distribution of cement based foam and its effect on thermal conductivity. *Journal Article* **2017**, *149*, 17.
(29) Li, T.; Huang, F.; Zhu, J.; Tang, J.; Liu, J. Effect of foaming gas and cement type on the thermal conductivity of foamed concrete. *Journal Article* **2020**, *231*, No. 117197.
(30) Shi, X.; Huang, J.; Su, Q. Experimental and numerical analyses of lightweight foamed concrete as filler for widening embankment. *Journal Article* **2020**, *250*, No. 118897.
(31) Li, G.; Tan, H.; He, X.; Zhang, J.; Deng, X.; Zheng, Z.; Guo, Y. The influence of wet ground fly ash on the performance of foamed concrete. *Journal Article* **2021**, *304*, No. 124676.
(32) Yu, Y.; Yu, L.; Fan, L.; Sun, L.; Zhang, Z. Effect of Mineral Admixtures on the Performance of Ceramsite Shotcrete for High Geothermal Underground Engineering. *Journal Article* **2022**, *7*, 5774.
(33) Masi, G.; Rickard, W. D. A.; Vickers, L.; Bignozzi, M. C.; van Riessen, A. A comparison between different foaming methods for the synthesis of light weight geopolymers. *Journal Article* **2014**, *40*, 13891.
(34) Zhou, W.; Zhang, Z.; Li, N.; Yan, W.; Ye, G. A new mullite foamed ceramic prepared by direct-foaming methods in parallel with a mechanical activation technique. *Journal Article* **2022**, *48*, 20721.
(35) Tanaka, S.; Takahashi, K.; Abe, M.; Noguchi, M.; Yamasaki, A. Preparation of High-Purity Calcium Carbonate by Mineral Carbonation Using Concrete Sludge. *Journal Article* **2022**, *7*, 19600.
(36) Medri, V.; Papa, E.; Dedecek, J.; Jirglova, H.; Benito, P.; Vaccari, A.; Landi, E. Effect of metallic Si addition on polymerization degree of in situ foamed alkali-aluminosilicates. *Journal Article* **2013**, *39*, 7657.
(37) Prud Homme, E.; Michaud, P.; Joussein, E.; Peyratout, C.; Smith, A.; Arrii-Clacens, S.; Clacens, J. M.; Rossignol, S. Silica fume as porogent agent in geo-materials at low temperature. *J. Eur. Ceram. Soc.* **2010**, *30*, 1641−1648.
(38) He, J.; Gao, Q.; Song, X.; Bu, X.; He, J. Effect of foaming agent on physical and mechanical properties of alkali-activated slag foamed concrete. *Journal Article* **2019**, *226*, 280.
(39) Hajimohammadi, A.; Ngo, T.; Mendis, P.; Sanjayan, J. Regulating the chemical foaming reaction to control the porosity of geopolymer foams. *Journal Article* **2017**, *120*, 255.
(40) She, W.; Du, Y.; Miao, C.; Liu, J.; Zhao, G.; Jiang, J.; Zhang, Y. Application of organic- and nanoparticle-modified foams in foamed concrete: Reinforcement and stabilization mechanisms. *Journal Article* **2018**, *106*, 12.
(41) Fei-fan, W.; Chuan-mei, D. U.; Jian-yong, P. Research on Performance of Thermal Insulation Materials in Underground High-temperature Tunnels. *Case Stud. Therm. Eng.* **2017**, *36*, 187.
(42) Ministry of housing and urban rural development of People's Republic of China. *Foam concrete*; China Construction Industry Press: The Beijing, 2011.

https://doi.org/10.1021/acsomega.3c06929
ACS Omega 2023, 8, 48091−48103